

AUTOMATED SPLIT HOPKINSON PRESSURE BAR FOR HIGH THROUGHPUT DYNAMIC EXPERIMENTS

Mouliswar Ramakumaresan*, Vladimir Kornev*, Pranav Kartha*, Isaac Faith Nahmad,
Suraj Ravindran

¹Department of Aerospace Engineering and Mechanics
University of Minnesota, Minneapolis, 55455

Corresponding author: sravi@umn.edu (Suraj Ravindran)

* These authors equally contributed to the work

Abstract

Background: Designing novel materials for impact applications and predicting material behavior using data-driven techniques require extensive datasets, which can be challenging to obtain through conventional experimental methods. While high throughput characterization is feasible at the sample micro and nanoscale, there remains a critical need for an experimental tool capable of facilitating high-throughput measurements at the macroscale.

Objective: This paper presents the design and development of a fully automated split Hopkinson pressure bar (SHPB) with full-field diagnostics for performing dynamic compression experiments on different materials.

Methods: The automated SHPB experiments consist of four main components: 1) striker launch and retrieval system, 2) bar repositioning mechanism, 3) automated sample placement system, and 4) diagnostics. Each of these systems employs various electromechanical devices and actuators programmed to work collaboratively to automate the SHPB experimental setup. A data analysis tool has been developed to automate the post-processing of the data obtained from the setup. The setup also incorporates automated high-speed imaging, enabling full-field strain measurement capabilities.

Results: To benchmark the setup, fully automated dynamic compression experiments were conducted on 45 Copper 101 samples and 20 3D-printed resin samples. The stress-strain curve was extracted from the raw data using the automated data analysis tool. The efficiency of the data analysis tool is validated by comparing the data with existing data analysis tools for SHPB. The stress-strain response obtained from the copper experiments aligned well with existing data on copper. Furthermore, the full-field strain measurements in experiments show strain values comparable to those of the strain gauge measurements.

Conclusion: This advancement has enabled dynamic compression experiments on materials at a rate of 60 samples per hour.

Keywords: Data-driven, materials design, high-throughput, automation, Hopkinson bar, dynamic compression, high strain rate

1. Introduction

Progress in data-driven methods and machine learning is revolutionizing the mechanics of materials research, particularly in constitutive modeling, material characterization, and the design of novel materials [1–4]. These methods require large data sets, which are often limited in the traditional experimental methods. Consequently, most of the current data-driven algorithms rely on the data obtained from numerical simulations to develop and validate advanced data-driven methods. While this approach is helping the progress of data-driven methods, it inherently limits the integration of novel physics from experiments into material models. It hinders the data-guided development of new materials based on the new mechanics of deformation and failure of the developed materials. High throughput experimentation offers a solution to overcome these limitations by generating diverse and extensive data sets suitable for data-driven methods.

There have been recent efforts focused on developing high-throughput experiments for characterizing materials across varying strain rates to screen the strength properties of materials for accelerating material discovery [5,6]. Most of these high throughput experimental methods in low and high-strain rate regimes are based on well-established nano-indentation and micro-indentation experiments. Indentation techniques typically measure force-displacement curves, which are then analyzed using Hertz's elastic solution to contact problems [7] or advanced inverse analysis for extracting the stress-strain curve of the materials from the force-displacement measurements [8,9]. These nano/micro indentation techniques are fast for screening the yield strength of materials; however, reliably measuring the large strain response of materials through these techniques is challenging. The main drawback of these techniques is that the data analysis is complex and prone to high errors when estimating tensile strength and other material properties beyond the yield strength of the materials [5]. Furthermore, the amount of material deformed in indentation techniques is minimal, which may not represent the continuum-scale behavior of the materials with microstructural heterogeneities at a larger length scale. In high strain rate regimes, indentation techniques have been implemented to study the material strength at strain rates ranging from 10^2 to 10^4 /s [10–13]. For strain rates exceeding 10^4 /s, laser-induced projectile impact testing (LIPIT) has been used to estimate the strength and damage in materials [14–17]. The high-strain-rate nano/micro indentation and LIPIT techniques have several drawbacks, including spatially non-uniform strain rates, complex stress states, and varying strain rates during loading and unloading.

Indentation and LIPIT-based experimental methods are crucial tools for the first-step evaluation of the material yield strength across varying strain rates. However, obtaining highly repeatable data on yield strength, tensile strength, and large strain behavior of material requires alternative strategies, such as automation of traditional experiments like uniaxial tension/compression for static loading and split Hopkinson pressure bar (SHPB) experiments for the high strain rate characterization. The primary challenge in these conventional experiments lies in the time-intensive process of loading, aligning, and rearming the testing apparatus after each experiment. Recently, the uniaxial compression experiments have been automated, and they can perform 1000s of experiments rapidly [18]. However, the conventional split Hopkinson pressure bar experiments used to characterize material strength at these high strain rates are challenging to automate due to the automation requirement of several processes involved in the experiment.

Several studies focused on developing impact fatigue devices, primarily addressing the rearming of the striker [19]. A great deal of development has been focused on automating the striker launch system, utilizing mechanisms such as vacuum systems or a rotary actuator. Isakov et al. used a

vacuum pump in the striker barrel to retract the striker bar, which was held in place using the incident bar with a shank [20]. This change in geometry causes a change in the shape of the input stress pulse, deviating from the desired square-shaped pulse. Quinn et al. implemented a flywheel mechanism to automate both the firing and retrieval of the striker bar, particularly for applications involving hazardous materials [21]. Additionally, in these experimental setups, samples are not reloaded, and bars are not repositioned, making high-throughput experimentation challenging. Therefore, conducting high-throughput experiments requires significant advancements in system design and automation.

The primary objective of this study is to develop an automated SHPB capable of performing large sets of experiments in the strain rate regime between 10^3 /s and 10^4 /s. The experimental setup has been designed and manufactured to systematically address the following challenges: (a) automatic re-arming of the striker bar to produce the desired compressive pulse; (b) self-regulated sample placement; (c) automated data acquisition and processing. Section 2 details the experimental setup and design of individual components, along with a summary of the fully automated data processing technique employed to post-process the data. Section 3 discusses the results obtained from experiments on copper and 3D-printed samples, followed by the conclusion.

2. Materials and Methods

2.1 Experimental setup and data analysis

A typical split-Hopkinson setup consists of three bars: a striker bar for generating a compressive stress pulse, an incident bar for carrying the pulse toward the sample, and a transmitter bar for carrying the stress pulse succeeding the deformation of the sample. Assuming force equilibrium in the sample, the following equations are used to obtain the stress, strain, and strain rate in the sample:

$$\text{Sample stress, } \sigma_s(t) = \frac{EA}{A_s} \varepsilon^T(t) \quad 1$$

$$\text{Sample strain, } \varepsilon_s(t) = \frac{-2C_0}{L_s} \int_0^t \varepsilon^R(t) dt \quad 2$$

$$\text{Strain rate, } \dot{\varepsilon}_s(t) = \frac{-2C_0}{L_s} \varepsilon^R(t) \quad 3$$

In the equations, ε^T , ε^R are the transmitted and reflected strain signals. Parameters A and A_s are the cross-sectional area of the bar and sample; E and C_0 are the Young's modulus and elastic wave speed in the bar material. In the present setup, strain gages are used as the diagnostic tool, where the two diametrically opposite gages on the incident bar measure the incident/reflected pulse, and the strain gages on the transmitter bar measure the transmitter strain pulse. The position of the two gages on the incident bar accounts for bending in the bar.

2.2 Automated experimental split Hopkinson pressure bar

A schematic of the fully automated split Hopkinson pressure bar (ASHPB) setup is shown in Fig.1. The ASHPB has four key components – the striker launch and retrieval system (SLRS), the bar repositioning system (BRS), the sample placement system (SPS), and the diagnostics. The SLRS is automated through various sensors and a network of solenoids connected through DC relays.

These DC relays are controlled by an AVR microcontroller that coordinates and regulates all four key components, providing communication during experiments. The BRS involves a collaborative effort between a linear stage actuator powered by a stepper motor and a servo motor (rotational motion) mounted onto the linear stage. The SPS comprises a linear stage actuator with a stepper motor (rotational motion), which is attached to a custom 3D-printed sample holder, enabling automated reloading of samples. The working of each component and the entire process involved in the experiments are discussed in the following sections. Two types of diagnostics are used in the experimental setup. First, the strain waves in the bars are measured using a set of strain gauges connected to an oscilloscope through a strain amplifier. A computer communicates through the NI-VISA framework to the oscilloscope to automate the data acquisition for any number of experiments. At the same time, a high-speed camera from Shimadzu (HPV-X2) was integrated into the experimental setup to obtain in-situ full-field deformation measurements. A novel algorithm was developed to automatically extract the stress-strain and strain rate in the sample from the strain gauge signals. The full-field strain field was extracted from the high-speed images using VIC-2D software from Correlated Solutions.

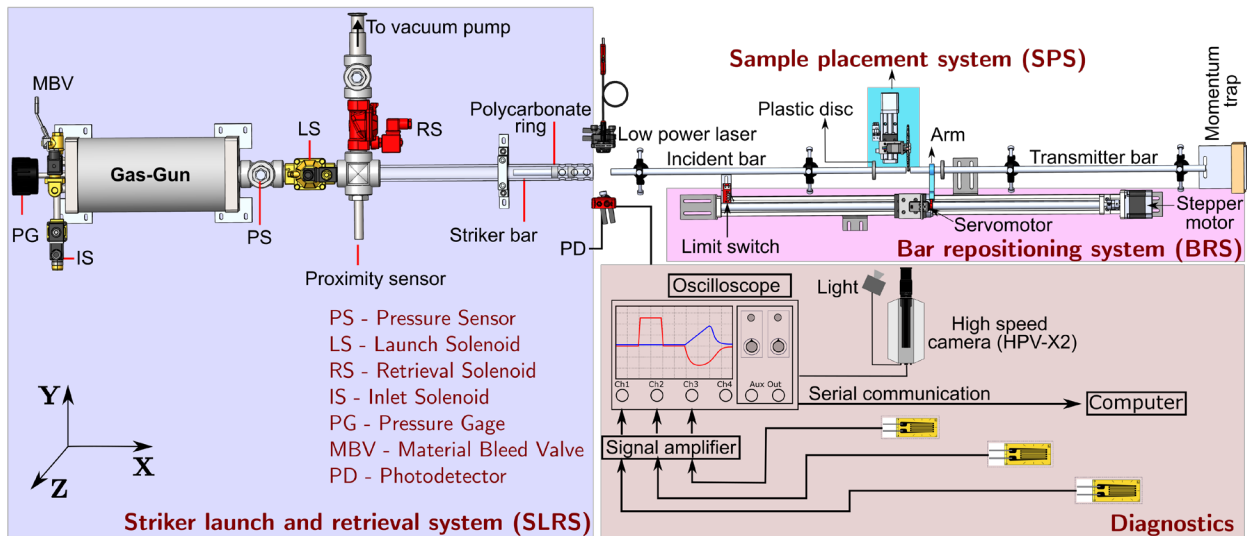


Fig. 1 Top view of rendered CAD of the complete mechanical system of Automated Split Hopkinson bar with the gas gun system, bar repositioning system, and sample placement system. (components are not to scale)

Two different materials were used for the experiments in this study: copper 101 (as received and annealed) and 3-D printed samples using the resin from FormLabs. For the experiments with copper samples, C350 maraging steel was used as the material for the striker, incident, and transmitter bars. However, for the experiments involving 3D-printed samples, aluminum was used for all three bars. This modification was necessary to obtain a measurable transmitter wave signal due to the low impedance of plastic samples. Incident and transmitter bars were fabricated to have a length of 1524 mm for aluminum and 1736 mm for maraging steel. Both types of bars have a diameter of 12.7 mm and centerless ground to have a uniform cross-section throughout their length. The entire ASHPB system was mounted on a set of optical tables reaching a total length of 5486.4 mm. To mount the bars, a custom machined brass ring was pressure fitted onto an optical ring mount from Edmund Optics (53 mm outer diameter, three screw adjustable, Part number: #03-

668), which was then screwed on the optical table by a post holder and clamp from Newport Corporation (VPH-2-P, PS-F-1.0C-PK).

2.3 Automated striker launch and retrieval system (SLRS)

The schematic of the automated gas gun system in the assembly is shown in Fig. 1. In contrast to the conventional gas-gun system, which only accelerates the striker bar to a specific velocity, the gas gun system developed in this study can also retract the striker bar to its initial position. The primary components of the system are a gas gun, a barrel, and a vacuum pump. The gas chamber is designed to hold gas pressures up to 250 psi, and the barrel has sufficient length for the striker bar to accelerate to the desired velocity. The internal diameter of the barrel is 40 mm, and the striker bar is 12.7 mm. Therefore, to ensure proper fit between the striker and the barrel, a polycarbonate ring with a diameter of 39.95 mm was press-fitted on the striker; see Fig. 1 (in SLRS). These rings were strategically designed to achieve a clearance fit to allow for the negative pressure differential between the open end of the barrel and the vacuum end when the vacuum pump is turned on during retrieval. Pressurization and bleeding of the gas gun, as well as launch and retraction of the striker bar, are regulated by using electromechanical solenoid valves. A high-pressure gas source fills the gas chamber with the help of an inlet solenoid valve (IS) and a pressure sensor (PS) from Amphenol Advanced Sensors (NPI-19J-300G2). A vacuum pump with a two-way retrieval solenoid (RS) retracts the striker bar after each experiment to its initial position by creating negative pressure behind the projectile. While the striker bar travels backward in the barrel, an infrared proximity sensor (Automation Direct: CD12L-0B-020-A0) detects the arrival of the striker bar. The proximity sensor ensures that the position of the striker bar is approximately the same for all the experiments to obtain the same impact velocity for a given pressure. Once the striker bar is retracted and the required pressure is attained in the gas chamber, the launch solenoid (LS) is actuated to release the compressed gas to launch the striker bar.

2.4 Bar Repositioning System

The Bar Repositioning System (BRS) is the drive unit that controls the entire setup to function in synchronization with each other. The BRS unit consists of 2 actuators to provide 2 degrees of freedom, as illustrated in Fig. 1. The first actuator is a linear motorized stage (FUYU Motion FSK40) controlled by a bipolar stepper motor. The travel length of this linear stage is 0.7 meters and has a resolution of 300 micrometers. The second actuator, a DC servomotor, is attached to the linear stage and has an allowed rotational range of 30° about the X-axis. A 3D-printed arm is connected to the servomotor, which can swing in and swing out when required. A polycarbonate ring is pressure fitted on the incident and transmitter bar to help in the translation of the bars with the 3D-printed arm attached to the servo motor. During the experiments, the bar repositioning system moves the incident bar towards the gas gun to push the striker bar back into the barrel. This push creates a proper seal between the barrel and the projectile to ensure a vacuum seal for retraction. Then, the incident bar is pushed forward to position the right end of the transmitter bar against the momentum trap, which ensures accurate positioning of the transmitter bar in every experiment. Following this, the incident bar is moved toward the barrel, and the sample placement system moves the samples toward the bars to sandwich the sample between the incident bar and the transmitter bar. Once the sample is sandwiched between the bars, the BRS moves the transmitter bar towards the barrel till the impact end of the incident bar reaches the low-power

laser. An AVR microcontroller controls the entire positioning of the incident and transmitter bar using an open loop control. It is referenced using a limit switch at one end of the linear stage. While the primary purpose of this microcontroller is to control the position of the incident and transmission bars, it also provides a signal to the SPS and, more importantly, acts as a master microcontroller to the gas gun system, which ensures the firing of the striker bar only after the sample is loaded.

2.5 Sample Placement System

The purpose of this system is to hold and feed samples between the incident and transmitter bars, see Fig. 2. The bar repositioning system controls the sample placement system (SPS). It has been built to have 2 degrees of freedom, one in the Y direction (perpendicular to the bars, see Fig.1) and the other is the rotation about X-axis. The SPS consists of a smaller motorized linear stage (FUYU Motion FSL30), actuated by a bipolar stepper motor which holds another high precision stepper motor (SOYO: SY20STH30-0604A) through an L-clamp as shown in Fig 2. A sample holder is attached to the high-precision stepper motor shaft with slots to load up to 20 samples. The sample holder is 3D printed using a soft material that is compliant and can provide gripping force to samples (6 mm × 6 mm × 4 mm) without damaging the surface finish or interfering with the working of the setup. Also, the thickness of the holder is smaller than the sample, see top view in Fig. 2, therefore, during the sample placement, the sample holder does not touch the incident and transmitter bars. The high-precision stepper motor allows for a new sample to be placed in between the incident and transmitter bar by rotating 15° to a new sample after every shot. After feeding a new sample, the cartridge is moved away from the incident, and transmission bars using the linear actuator to keep the compliant sample holder from being damaged during the shot. The sample holder is fully loaded with a new set of samples after testing all the previous sets of samples. Although the sample holder, with a diameter of 85 mm, has been designed to hold up to 20 samples, it is possible to increase this number by either increasing the diameter of the compliant member and/or by reducing the sample size.

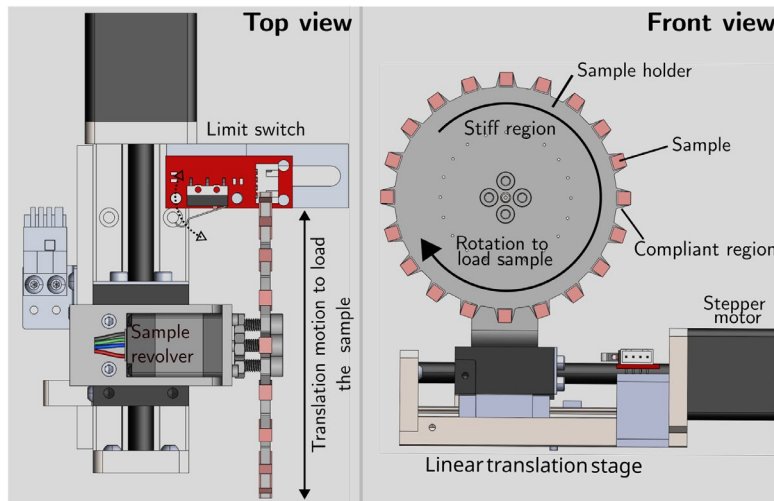


Fig. 2 Top and front view of sample placement system.

2.6 Data acquisition and automated data analysis

The diagnostics system is an independent unit that consists of a laser source (from Thorlabs, PL202), a photodetector (from Thorlabs, PDA10A2), a 2-series Tektronix MSO, strain gages, and a high-speed Shimadzu HPV-X2 camera for *in-situ* digital image correlation (DIC). This unit is designed to perform two main functions: capture the signals from strain gages to save the corresponding signals for post-processing and, in addition, provide a trigger signal to the camera to capture data for DIC. The entire operation is controlled using a Python script that communicates with the oscilloscope during experiments using serial communication. The laser source and photodetector provide the first signal to the oscilloscope to begin data acquisition upon arrival of the striker bar.

A MATLAB script post-processes the data from a series of CSV files collected during the experiment, each containing raw strain gauge measurements corresponding to an individual shot. The script iteratively reads and processes each shot, saving the results to an Excel file and generating consolidated figures simultaneously. Processing begins with removing bias in the raw voltage measurements from the strain gauges and denoising using a moving average filter containing 10 data points (significantly smaller than the size of strain pulses, ~2000 data points). After that, the voltages from the strain gauges are converted to strain using the appropriate conversion factor. Through multiple steps, an algorithm then isolates the incident, transmitted, and reflected signals from the incident and transmitter bars' strain data while also correcting for wave dispersion. This begins by determining the data indices corresponding to the start, first peak, and end of the incident and reflected signals. The start of a signal is found when strain values first pass a signal threshold and then back-track data indices until values reach a zero threshold. The first peak was found by determining when strain readings after the signal threshold began to decrease in magnitude. The algorithm would then determine the end of a signal by looking for when data once again reached the zero threshold after the first peak. The signal and zero thresholds are sign-dependent in accounting for the incident and reflected signals appearing on the same strain gauge channel. As a result, the algorithm parses through the incident bar data twice, flipping the sign when looking for the reflected signal.

With the key data indices for the incident and reflected signals, all three signals can be picked out and aligned from the incident and transmitter bar strain data. However, this alignment is only preliminary as wave dispersion causes a stretching of the reflected and transmitted signal compared to the incident signal, and dispersion correction will cause a shifting of data, requiring realignment. This calls for the signals to be captured with a buffer to ensure that no data is lost after dispersion correction and that there are enough data points that the dispersion-corrected signals can be properly cropped. This is accomplished by determining the rise time of the incident and reflected signals. The larger one determines which corresponding signal acts as the baseline, which will be referred to as the reference signal against which the other signal is aligned. The reference signal is cropped from the incident bar strain data by capturing a rise time's worth of data ahead and behind the signal's start and end, respectively, to capture the whole pulse with a buffer. The beginning of the other signal is picked out by capturing data from two reference signal rise times ahead of its peak. The end is found by capturing data that matches the amount of data points from the reference signal's peak to its signal end plus buffer. As a result, the incident and reflected signals are captured with the peaks aligned with a buffer ahead and behind the signals. The transmitted signal is captured by keeping its alignment with the reflected signal and cropping it to the same size. Lastly,

the time series is recreated from the start of all the captured signals and continues until the end of the signals.

Dispersion correction is done on the signals with a buffer using Bancroft's dispersion relationship and the process described in [22]. To characterize Bancroft's dispersion data, the curve fitting parameters corresponding to Poisson's Ratio of the incident and transmitter bars were used [23]. This curve fit describes the dispersion relationship and allows for the determination of the phase velocity for each Fourier component of a pulse, in this case, up to the 50th component, which is used to find the phase increment for each component. The Fourier expansion of the signals is determined, and the incident signal is propagated forward, while the reflected and transmitted signals are propagated backward using the found phase increments. The signals, now dispersion corrected, are converted back into the time domain and aligned with each other in the same manner as before; however, with no buffer surrounding the signals. With the fully processed incident, transmitted, and reflected strain signals, quantities of interest (stress, strain, strain rate, etc.) are calculated for each shot and aggregated.

2.6 Process synchronization and complete experimental workflow

The schematics of the process synchronization and experimental workflow are shown in Fig. 3. All the solenoids and the vacuum pump are controlled by DC relays (Songle: SRD-05VDC-SL-C), which are connected to a slave AVR microcontroller. A master AVR microcontroller from the BRS controls this slave microcontroller, which allows for synchronous and collaborative operation of BRS, SPS, BLRS, and diagnostics.

The automation begins with the BRS, which translates the incident and transmitter bar to allow the sample placement system to position the sample between them. Both the BRS and SPS rely on limit switches (L1 and L2) to position the actuator stages, ensuring that the incident and transmitter bars return to their preset axial coordinates after each experiment. During the repositioning of the bar with the help of the BRS, the incident bar is moved towards the gun, pushing the striker into the barrel to facilitate its retraction. Following this process, the BRS pushes the incident bar forward, causing it to contact and push the transmitter bar until it reaches the momentum trap at the far-right end. After that, the incident bar is again pushed backward to make the space between the incident and transmitter for the placement of the sample. At this point, the SPS gets the signal from the master controller to move forward and places the sample between the incident and transmitter bars. Once the sample comes between the bars, the BRS moves the incident bars forward, which pushes the sample against the transmitter bar with a small force. At this point, the master controller sends a signal to the SPS, which essentially loads the sample between the bars (see the video in the supplementary for the complete process). Once the sample is loaded and the impact end of the incident bar is placed at the low-power laser, the master controller transmits a signal to the slave controller to take control of the striker launch and retrieval system (SLRS). The vacuum pump attached to the barrel starts operating along with the open-retrieval solenoid (RS), creating a low pressure behind the striker that allows the retraction of the striker bar. At one end of the barrel connected to the pressure tank, a pressure sensor (PS) and proximity sensor (P1) are used to verify the pressure in the gas chamber and the location of the striker bar, respectively. The proximity sensor detects the presence of the striker bar as it is fully retracted. The signal from the proximity sensor shuts the retrieval solenoid valve (RS) and deactivates the vacuum pump. The gas chamber is pressurized to the required level by actuating the gas inlet solenoid valve (IS). Following this, the launch solenoid (LS) is actuated to launch the striker bar. A photodetector is

positioned precisely before the plane where the striker bar impacts the incident bar. The output change from the photodetector triggers the oscilloscope to record strain gauge signals from the incident and transmitter bar, and the Python script saves it automatically to an external flash drive. The entire process is programmed to run till all the samples are tested. The data from the strain gages are then imported into the MATLAB script to post-process the data and generate batch reports. In the experiments with integrated high speed imaging, the cameras are triggered by the Photodetector (PD, shown in Fig. 2), as discussed in the previous sections. The camera automatically resets after every shot, using the PYAUTOGUI library in Python to capture the images for the following experiment. These images are saved on the computer automatically and later used for post-processing.

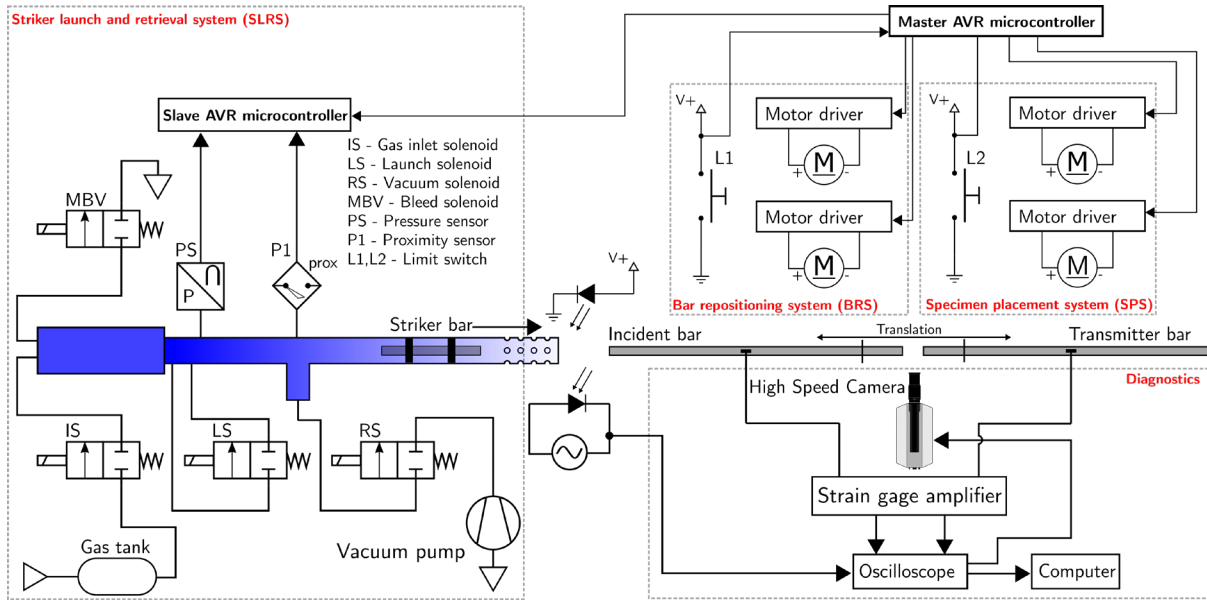


Fig 3 Schematic showing experimental workflow for one batch of sample

3. Results and Discussion

To validate and benchmark the experimental setup, three sets of experiments with two different materials were performed on Cu101 and 3D-printed resin samples. A total of 40 samples were prepared from Cu101, comprising 20 as received and 20 annealed under an inert Argon gas atmosphere at a temperature of 370°C for 60 minutes. In addition, 20 samples were 3D printed using a FormLabs 3 printer, followed by gentle polishing using 800-grit paper, and washed with acetone to obtain a clean surface. The pressure in the gas chamber was programmed to reach 25 PSI for Cu101 and 15 PSI for the 3D-printed samples during each shot. A pressure gauge (PG, shown in Fig. 2) was used to physically verify the pressure in the chamber for each shot when needed. This was done for two purposes: (1) to verify that the pressure sensor (PS, shown in Fig. 2 and Fig. 3) is calibrated; (2) to map the changes in the pressure for each shot and correlate it with the post-processed data, such as strain rate, true stress, and true strain. The raw signals from the experiment were post-processed using an automated data analysis tool, as discussed in the previous section, to appropriately clip and time shift the incident, reflected, and transmitted pulses for calculating the true stress-true strain and the strain rate in the samples.

3.1 Dynamic compression of Cu101

Copper has been extensively studied under various strain rate conditions, and in this study, it serves as a benchmark for the Hopkinson bar setup [24–30]. Two batches of Cu101 were precisely manufactured to a gauge length of 4 mm and mounted on the sample holder. The dimensional accuracy of each sample, along the gauge length, was ± 0.05 mm, with surface flatness maintained at ± 0.1 mm on all faces. A successful automated experiment was defined by meeting three key objectives: (a) loading the sample co-axially between the bars; (b) pressurizing the chamber to the programmed value; (c) successfully capturing and saving the incident, reflected and transmitter bar strain signals for post-processing.

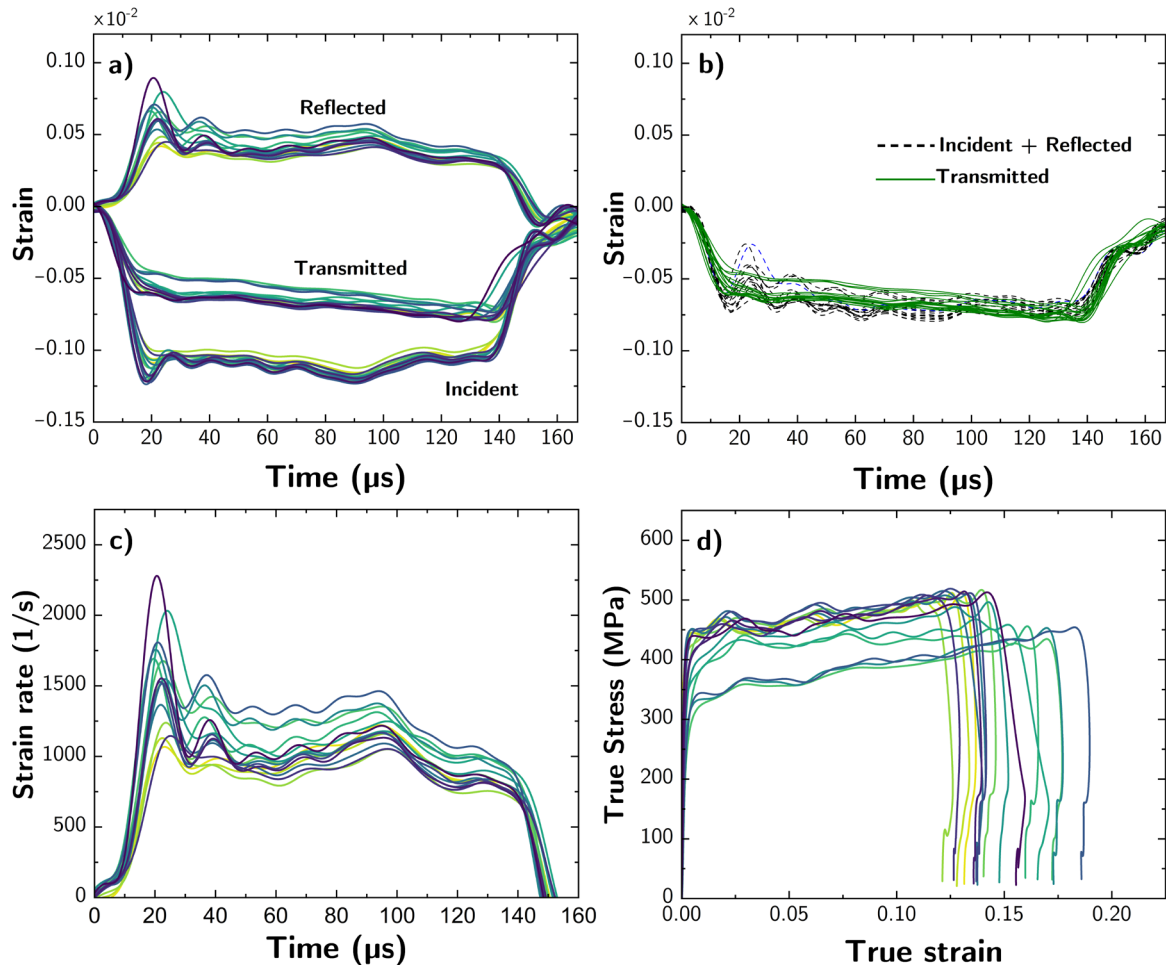


Fig 4 Post-processed data from as received Cu 101 (a) Strain gage signals as a function of time (b) Force equilibrium in the sample (c) variation of strain rate with time (d) stress-strain response of samples.

In the first batch of experiments with as-received Cu101, 16 out of 20 experiments were successful, with a total experimental runtime of 19 minutes. Fig. 4a shows the strain gauge signals from the incident and transmitter bars, which are clipped using the automated data analysis tool developed in this study. Force equilibrium in the SHPB experiments is essential for calculating reliable stress-

strain response from the strain gauge signals measured in the incident and transmitter bar. The sum of the incident and reflected signals (corresponding to force on the left side of the sample) and the transmitter signals (corresponding to force on the right side of the sample) for all the experiments conducted on the as-received Cu101 are plotted in Fig.4b. These plots show the attainment of force equilibrium in all experiments conducted on the Cu101 samples. The average strain rates reached in as-received Cu101 was found to be 1074 /s, with a standard deviation of 124 /s, see Fig.4b. Summary of the flow strength at different strains and their standard deviation are shown in Table. A high variability in stress-strain response was observed in these experiments, as seen in Fig 4d, which shows mainly two sets of stress-strain curves with a mean peak flow stress of 450 MPa and 370 MPa at 10 % strain.

Table 1 Summary of experiments on as-received Cu 101 samples

Parameters	Mean	Standard Deviation
Average strain rate	1074.12 /s	125 /s
Stress at 2% strain	396.47 MPa	74.65 MPa
Stress at 5% strain	429.02 MPa	37.81 MPa
Stress at 10% strain	453.26 MPa	34.65 MPa
Stress at 15% strain	439.44 MPa	24.30 MPa
Stress at 20% strain	412.37 MPa	28.97 MPa

In a conventional Hopkinson bar, the variability in stress-strain response could be attributed to variations in striker bar velocity, improper sample placement, diagnostic errors in strain gauge instrumentation, or inconsistencies in sample preparation. However, since the entire setup has been automated, it is highly unlikely that these variations are due to striker bar velocity as the pressure in the gas chamber reaches the programmed pressure within ± 1.5 PSI. Additionally, the pressure in the gas chamber was recorded through the pressure gauge and was found to be within ± 1.5 PSI for each shot. Issues with sample placement and diagnostics are also unlikely as the sample placement system and diagnostics calibrate themselves after each shot and have demonstrated high precision (see supplementary data for a video showing sample placement for 20 shots). This leaves the only reasonable explanation for this variation to be due to variation in the sample geometry or its inherent microstructure. As mentioned previously, the dimensions of each sample were checked and were found to be within ± 0.05 mm tolerance, which cannot be the reason for the significant variation. Therefore, the only possibility for the variability in stress-strain response may be coming from the different processing routes of the as-received Cu101. Cu101 can have different hardness ratings depending on the processing, which can significantly affect the stress-strain response. This hypothesis is tested by performing experiments on annealed Cu101 samples. In the annealed Cu101 experiments, 14 experiments were successful out of 20 experiments with a runtime of 19 minutes. The stress-strain response from the annealed sample is shown in Fig. 5c, which shows a considerable improvement in the consistency between each shot with the annealed Cu101. The mean strain rate from Fig. 5b was 1959 /s, with a standard deviation of 56.23 /s. The mean stress at various strains for annealed Cu 101 Table 2 shows the variability between the experiments is within 3 %. The true stress-strain of annealed Cu101 throughout the deformation is found to be highly repeatable across all samples. The nominal grain size, after etching and examining under an optical microscope, was calculated to be 22 micrometers, which corresponds well with its stress-strain flow curve according to the previous study by Meyer et al. [30]. To understand the

efficacy of the developed automated code, a well-established SHPB data processing software from Francis et al. [17] was used to post-process one batch of experiments with a Hopkinson bar analysis code and compared with the corresponding automated MATLAB script results, as shown in Fig. 5d. These results confirm that the automated data analysis tool developed in our study reliably calculated the stress-strain response.

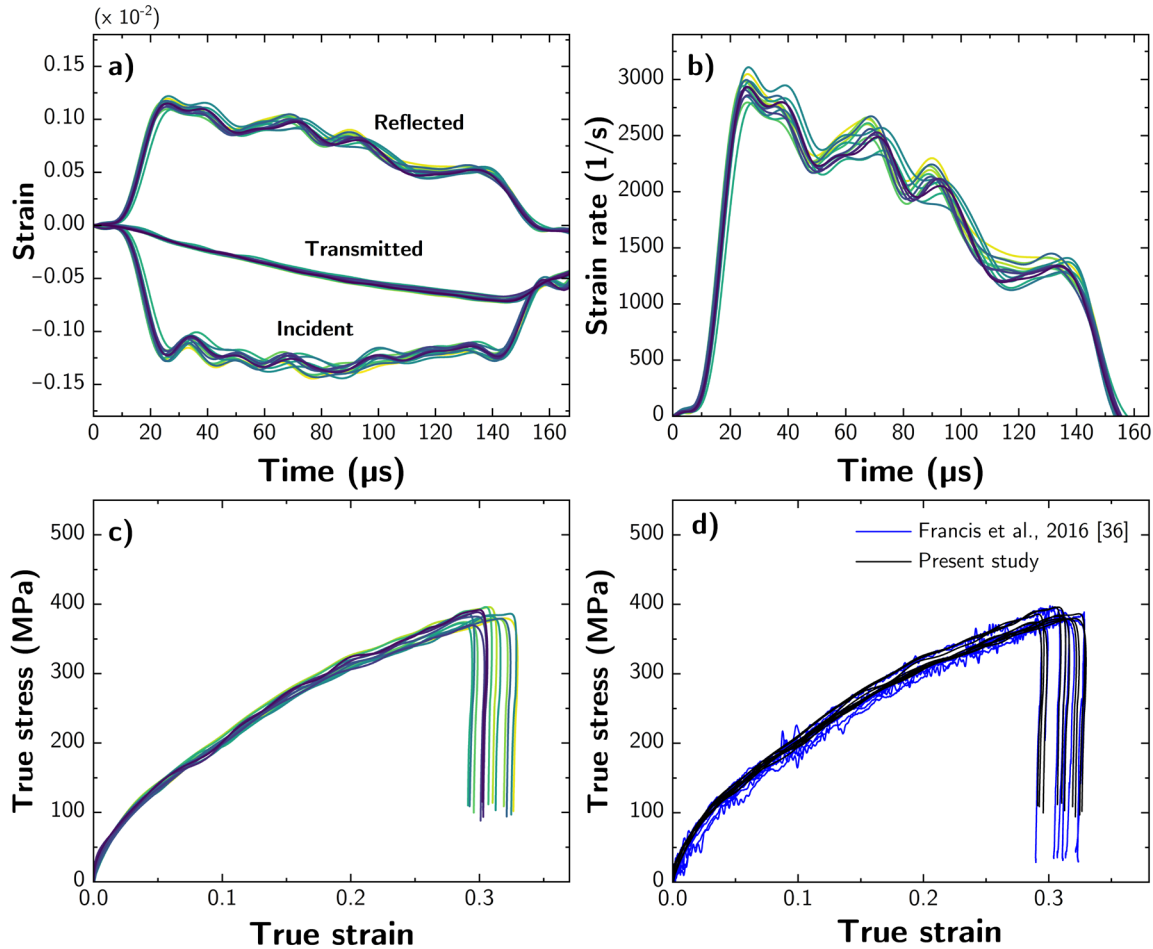


Fig 5 Post-processed data from annealed Cu 101 (a) Strain gage signals as a function of time (b) Variation of strain rate with time (c) Stress-Strain response of samples (d) Comparison of stress-strain curve between Genetic Algorithm aided analysis (Francis et al.) and automated MATLAB code.

Table 2 Summary of experiments on annealed Cu101 samples

Parameters	Mean	Standard Deviation
Average strain rate	1958 /s	56.23 /s
Stress at 2% strain	81.19 MPa	3.36 MPa
Stress at 5% strain	136.21 MPa	4.46 MPa
Stress at 10% strain	201.16 MPa	4.55 MPa
Stress at 15% strain	265.55 MPa	6.32 MPa
Stress at 20% strain	314.24 MPa	7.15 MPa

3.2 Automated dynamic compression experiments with full-field measurements

While strain gages are widely used in SHPB experiments, obtaining spatially resolved data is essential for solving many engineering problems. One-dimensional stress-strain data alone does not provide sufficient data for developing data-driven material models. There are new data-driven techniques that utilize full-field displacement/strain data for discovering material models, which motivates the requirements of full-field measurements [31,32]. Therefore, it is necessary to develop automated high speed full-field imaging with digital image correlation capability, which can provide spatially resolved displacement and strain fields [33–35]. To achieve this, a high-speed Shimadzu HPVX-2 camera was integrated into the existing test setup to provide spatially resolved measurements for every experiment through automated 2D DIC measurements, see Fig. 6a. The samples are speckled to facilitate the DIC measurements during loading. The images obtained from the experiment were post-processed using commercial software called Vic-2D from Correlated Solutions. Fig. 6a shows the full-field strain evolution for three samples at similar strain rates. The axial strain is relatively homogeneous for all the experiments, which is an assumption in the one-dimensional analysis of waves in SHPB. Fig 6b shows the average and standard deviation of axial strain for 5 experiments performed using DIC and compared with strain evolution from the strain gage analysis. Both strain measurements correspond with each other, with a slight deviation at about 80 μs . Such observations in material behavior mainly come from the assumptions involved in 1-D wave analysis. All these experiments are fully automated, including the camera, which allows a unique opportunity to develop extensive data from dynamic experiments.

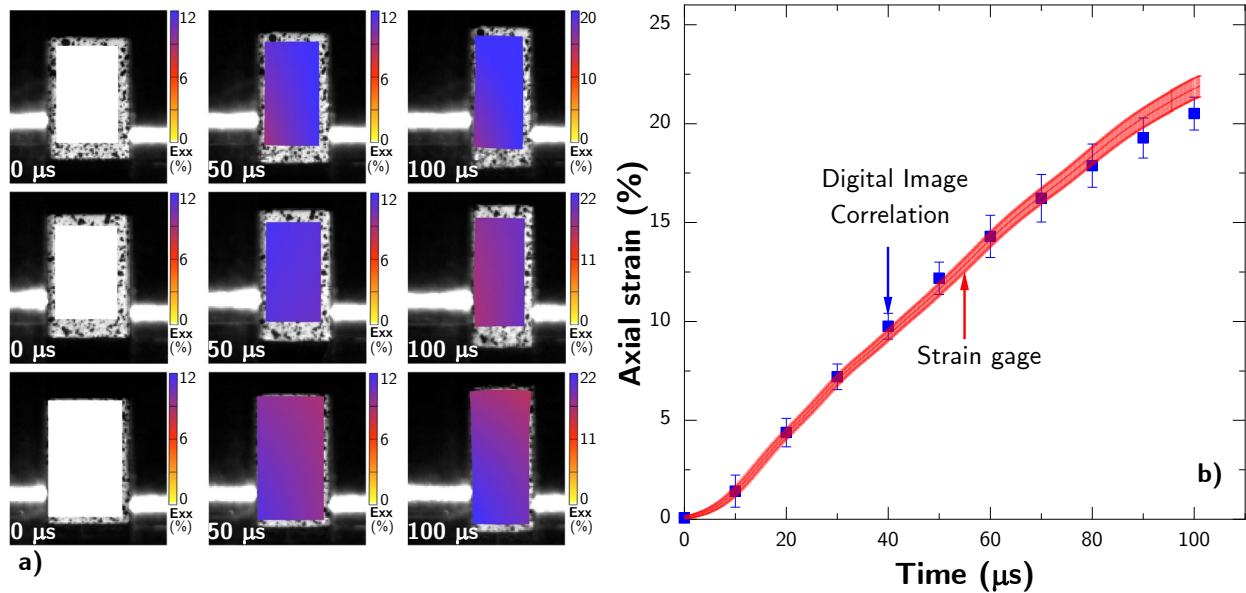


Fig 6 a) Full-field axial strain at three different times $t = 0 \mu\text{s}$, $50 \mu\text{s}$ and $100 \mu\text{s}$, b) average axial strain evolution from high speed DIC and strain gages in the incident and transmitter bars.

3.2 Dynamic compression of 3D-printed resin

Fig. 7a shows the variation of incident, reflected, and transmitted strain gage signals plotted as a function of time. Out of 20 samples, data was successfully obtained for 12 samples with an experimental runtime of 19 min. The plot between strain rate and time, in Fig 7c, shows an average strain rate of 1857.17 /s with a standard deviation of 161.77 /s. The associated true stress versus true strain response of the samples is shown in Fig. 7d where the peak stress is observed across all samples. The mean true stress observed at a strain of 5% is 152.21 MPa with a standard deviation of 8.55 MPa. The general trend, as observed in Fig. 7d, shows scattered signals from all the samples tested in a single batch. Table 3 provides a quantitative analysis of the experimental results. The variability in the stress-strain response of the samples can likely be attributed to the differences in curing rate. However, this variation presented challenges as several factors needed to be considered, including exposure time to external light and print defects that arise during cleaning.

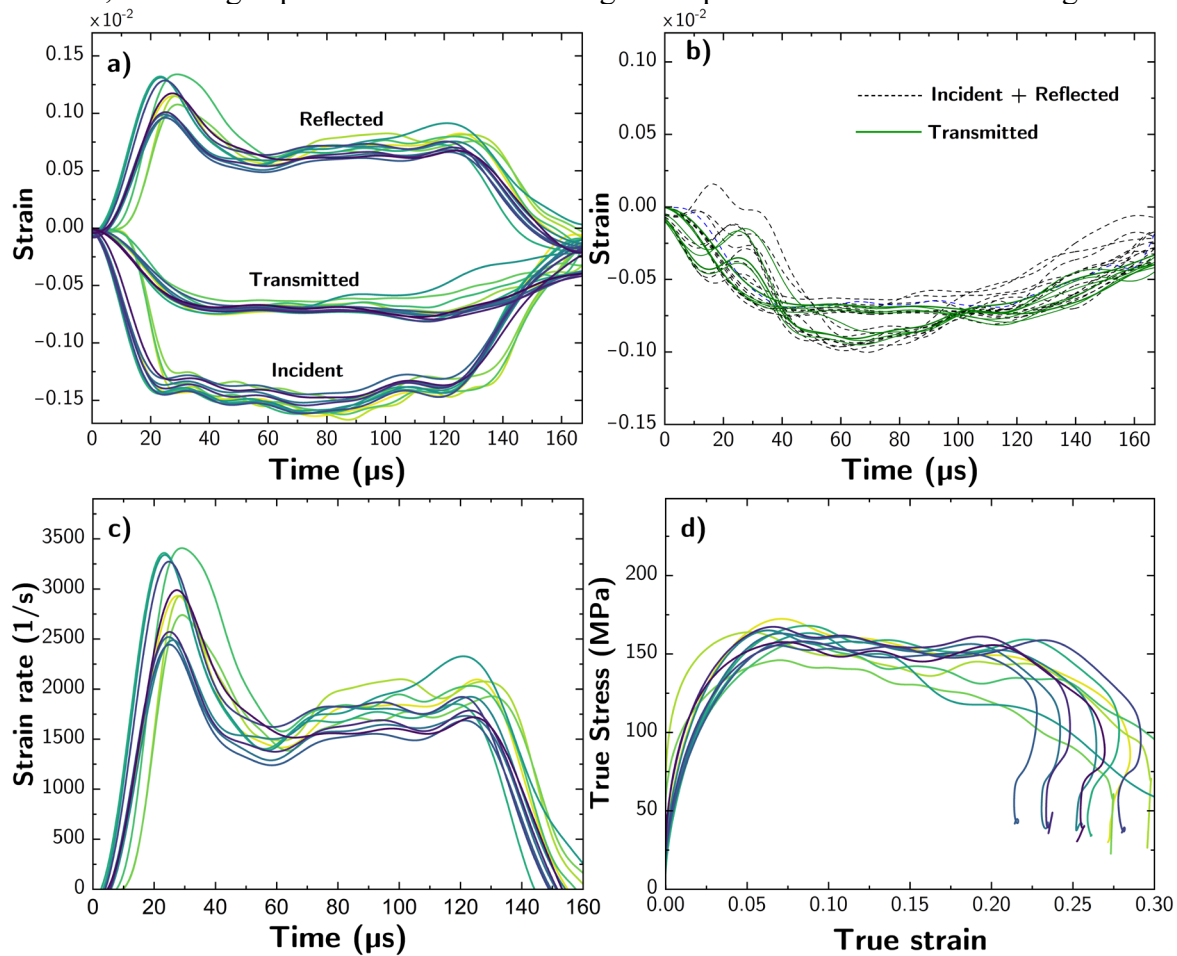


Fig 7 Post-processed data from one batch of 3D printed samples (a) strain gauge signals as a function of time (b) force equilibrium in the sample (c) variation of strain rate with time (d) stress-strain response of samples.

Table 3 Summary of experiments on 3D printed resin samples

Parameters	Mean	Standard Deviation
Average strain rate	1857.17 /s	161.69 /s
Stress at 2% strain	113.23 MPa	14.33 MPa
Stress at 5% strain	152.21 MPa	8.55 MPa
Stress at 10% strain	155.55 MPa	6.75 MPa
Stress at 15% strain	147.31 MPa	7.81 MPa
Stress at 20% strain	144.64 MPa	14.08 MPa

4. Conclusion

In this study, a fully automated split Hopkinson bar setup with full-field high speed measurements was developed to generate extensive data sets of dynamic compression experiments. This experimental setup is capable of performing 60 dynamic compression experiments per hour. A MATLAB script was written to accelerate the post-processing of the raw data generated from the experiments. The script was able to process raw data effectively, and the resulting stress-strain responses compare well with those obtained using existing Hopkinson bar data analysis software. To benchmark the setup, experiments were conducted on as-received and annealed Cu101 samples. The annealed Cu101 sample data shows highly repeatable measurements with minimal variation in the stress-strain response at a given strain rate. In addition, high-speed imaging was integrated into the experimental setup to facilitate DIC measurements and obtain large data sets of strain measurements at high strain rates. Further experiments on 3D printed samples have shown promising results, indicating the potential of this setup for generating large volumes of data from polymeric materials.

Acknowledgments

Funding support from the University of Minnesota is greatly acknowledged.

Conflict of Interest

We have no conflict of interest to disclose.

References

- [1] K. Karapiperis, L. Stainier, M. Ortiz, J.E. Andrade, Data-Driven multiscale modeling in mechanics, *Journal of the Mechanics and Physics of Solids* 147 (2021) 104239. <https://doi.org/10.1016/j.jmps.2020.104239>.
- [2] M. Mozaffar, R. Bostanabad, W. Chen, K. Ehmann, J. Cao, M.A. Bessa, Deep learning predicts path-dependent plasticity, *Proc. Natl. Acad. Sci. U.S.A.* 116 (2019) 26414–26420. <https://doi.org/10.1073/pnas.1911815116>.
- [3] T. Kirchdoerfer, M. Ortiz, Data-driven computational mechanics, *Computer Methods in Applied Mechanics and Engineering* 304 (2016) 81–101.
- [4] B. Liu, N. Kovachki, Z. Li, K. Azizzadenesheli, A. Anandkumar, A.M. Stuart, K. Bhattacharya, A learning-based multiscale method and its application to inelastic impact problems, *Journal of the Mechanics and Physics of Solids* 158 (2022) 104668.
- [5] S. Mohan, N. Millan-Espitia, M. Yao, N.V. Steenberge, S.R. Kalidindi, Critical Evaluation of Spherical Indentation Stress-Strain Protocols for the Estimation of the Yield Strengths of Steels, *Exp Mech* 61 (2021) 641–652. <https://doi.org/10.1007/s11340-021-00689-7>.

- [6] S. Shen, H. Li, L. Yang, N. Li, J. Wu, T. Zhao, High-throughput screening the micro-mechanical properties of polyimide matrix composites at elevated temperatures, *Polymer Testing* 107 (2022) 107483. <https://doi.org/10.1016/j.polymertesting.2022.107483>.
- [7] H. Hertz, *Miscellaneous Papers*, Macmillan, 1896.
- [8] T. Nakamura, T. Wang, S. Sampath, Determination of properties of graded materials by inverse analysis and instrumented indentation, *Acta Materialia* 48 (2000) 4293–4306. [https://doi.org/10.1016/S1359-6454\(00\)00217-2](https://doi.org/10.1016/S1359-6454(00)00217-2).
- [9] Y. Gu, T. Nakamura, L. Prchlik, S. Sampath, J. Wallace, Micro-indentation and inverse analysis to characterize elastic–plastic graded materials, *Materials Science and Engineering: A* 345 (2003) 223–233. [https://doi.org/10.1016/S0921-5093\(02\)00462-8](https://doi.org/10.1016/S0921-5093(02)00462-8).
- [10] J. Lu, S. Suresh, G. Ravichandran, Dynamic indentation for determining the strain rate sensitivity of metals, *Journal of the Mechanics and Physics of Solids* 51 (2003) 1923–1938. <https://doi.org/10.1016/j.jmps.2003.09.007>.
- [11] G. Subhash, H. Zhang, Dynamic indentation response of ZrHf-based bulk metallic glasses, *Journal of Materials Research* 22 (2007) 478–485. <https://doi.org/10.1557/jmr.2007.0058>.
- [12] J.D. Clayton, D.T. Casem, J.T. Lloyd, E.H. Retzlaff, Toward Material Property Extraction from Dynamic Spherical Indentation Experiments on Hardening Polycrystalline Metals, *Metals* 13 (2023) 276. <https://doi.org/10.3390/met13020276>.
- [13] Y. Zhang, B. Hackett, J. Dong, K. Xie, G. Pharr, Evolution of dislocation substructures in metals via high-strain-rate nanoindentation, *Proceedings of the National Academy of Sciences of the United States of America* 120 (2023) e2310500120. <https://doi.org/10.1073/pnas.2310500120>.
- [14] J.-H. Lee, D. Veysset, J.P. Singer, M. Retsch, G. Saini, T. Pezeril, K.A. Nelson, E.L. Thomas, High strain rate deformation of layered nanocomposites, *Nature Communications* 3 (2012) 1–9.
- [15] M. Razavipour, B. Jodoin, Material Model for Predicting Dynamic Response of Copper and Nickel at Very High Strain Rates Under Cold Spray Conditions, *J Therm Spray Tech* 30 (2021) 324–343. <https://doi.org/10.1007/s11666-020-01137-z>.
- [16] D. Veysset, J.-H. Lee, M. Hassani, S.E. Kooi, E.L. Thomas, K.A. Nelson, High-velocity micro-projectile impact testing, *Applied Physics Reviews* 8 (2021).
- [17] J. Ochilov, P. Yip, F.N. Shireman, S.J. Poovathingal, T. Schwartzenruber, S. Ravindran, Laser-Driven Microparticle Impact Experiments on Reinforced Carbon-Carbon, Graphite, and Silicon Carbide, in: 2025: p. 2455.
- [18] A.E. Gongora, K.L. Snapp, R. Pang, T.M. Tiano, K.G. Reyes, E. Whiting, T.J. Lawton, E.F. Morgan, K.A. Brown, Designing lattices for impact protection using transfer learning, *Matter* 5 (2022) 2829–2846. <https://doi.org/10.1016/j.matt.2022.06.051>.
- [19] S.J. Pagano, P.A. Jewell, L.E. Lamberson, A tunable modified-Hopkinson impact fatigue device, *Review of Scientific Instruments* 90 (2019).
- [20] M. Isakov, Cyclic Impact Test with the Hopkinson Bar: Application to Granite, *Journal of Dynamic Behavior of Materials* 10 (2023) 75–91. <https://doi.org/10.1007/s40870-023-00401-x>.
- [21] R.M. Quinn, L.H. Zhang, M.J. Cox, D. Townsend, T. Cartwright, G. Aldrich-Smith, P.A. Hooper, J.P. Dear, Development and Validation of a Hopkinson Bar for Hazardous Materials, *Experimental Mechanics* 60 (2020) 1275–1288. <https://doi.org/10.1007/s11340-020-00638-w>.

- [22] J.M. Lifshitz, H. Leber, Data processing in the split Hopkinson pressure bar tests, *International Journal of Impact Engineering* 15 (1994) 723–733. [https://doi.org/10.1016/0734-743X\(94\)90011-9](https://doi.org/10.1016/0734-743X(94)90011-9).
- [23] B.A. Gama, S.L. Lopatnikov, J.W. Gillespie, Hopkinson bar experimental technique: A critical review, *Applied Mechanics Reviews* 57 (2004) 223–250. <https://doi.org/10.1115/1.1704626>.
- [24] T. Suo, Y. Li, F. Zhao, X. Fan, W. Guo, Compressive behavior and rate-controlling mechanisms of ultrafine grained copper over wide temperature and strain rate ranges, *Mechanics of Materials* 61 (2013) 1–10. <https://doi.org/10.1016/j.mechmat.2013.02.003>.
- [25] V. Dupont, T.C. Germann, Strain rate and orientation dependencies of the strength of single crystalline copper under compression, *Phys. Rev. B* 86 (2012) 134111. <https://doi.org/10.1103/PhysRevB.86.134111>.
- [26] D. Rittel, G. Ravichandran, S. Lee, Large strain constitutive behavior of OFHC copper over a wide range of strain rates using the shear compression specimen, *Mechanics of Materials* 34 (2002) 627–642. [https://doi.org/10.1016/S0167-6636\(02\)00164-3](https://doi.org/10.1016/S0167-6636(02)00164-3).
- [27] U. Andrade, M.A. Meyers, K.S. Vecchio, A.H. Chokshi, Dynamic recrystallization in high-strain, high-strain-rate plastic deformation of copper, *Acta Metallurgica et Materialia* 42 (1994) 3183–3195. [https://doi.org/10.1016/0956-7151\(94\)90417-0](https://doi.org/10.1016/0956-7151(94)90417-0).
- [28] A. Mishra, M. Martin, N.N. Thadhani, B.K. Kad, E.A. Kenik, M.A. Meyers, High-strain-rate response of ultra-fine-grained copper, *Acta Materialia* 56 (2008) 2770–2783. <https://doi.org/10.1016/j.actamat.2008.02.023>.
- [29] S. Ravindran, V. Gandhi, Z. Lovinger, M. Mello, G. Ravichandran, Dynamic Strength of Copper at High Pressures Using Pressure Shear Plate Experiments, *J. Dynamic Behavior Mater.* 7 (2021) 248–261. <https://doi.org/10.1007/s40870-020-00287-z>.
- [30] M.A. Meyers, U.R. Andrade, A.H. Chokshi, The effect of grain size on the high-strain, high-strain-rate behavior of copper, *Metall Mater Trans A* 26 (1995) 2881–2893. <https://doi.org/10.1007/BF02669646>.
- [31] A. Akerson, A. Rajan, K. Bhattacharya, Learning constitutive relations from experiments: 1. PDE constrained optimization, arXiv Preprint arXiv:2412.02864 (2024).
- [32] M. Flaschel, S. Kumar, L. De Lorenzis, Automated discovery of generalized standard material models with EUCLID, *Computer Methods in Applied Mechanics and Engineering* 405 (2023) 115867.
- [33] M.A. Sutton, J.J. Orteu, H. Schreier, Image correlation for shape, motion and deformation measurements: basic concepts, theory and applications, Springer Science & Business Media, 2009.
- [34] S. Ravindran, V. Gandhi, A. Joshi, G. Ravichandran, Three-dimensional full-field velocity measurements in shock compression experiments using stereo digital image correlation, *Review of Scientific Instruments* 94 (2023).
- [35] S. Ravindran, B. Koohbor, P. Malchow, A. Kidane, Experimental characterization of compaction wave propagation in cellular polymers, *International Journal of Solids and Structures* 139 (2018) 270–282.